Thermal-lensing measurement of particle thermophoresis in aqueous dispersions

Roberto Rusconi, Lucio Isa, and Roberto Piazza

Dipartimento di Ingegneria Nucleare, Politecnico di Milano via Ponzio 34/3, 20133 Milano, Italy

Received July 24, 2003; revised manuscript received October 21, 2003; accepted November 4, 2003

We show that thermophoresis (particle drift driven by thermal gradients) in aqueous solutions can be measured by using an all-optical thermal-lensing setup, where a temperature gradient is set by a near-infrared laser beam with no need of light-absorbing dyes. After discussing the principles of the method, we study by numerical simulation the nature and extent of parasitic thermal-convection effects, and we describe an optical setup designed to limit them. We finally present preliminary results on thermophoresis in micellar solutions and colloidal dispersions. © 2004 Optical Society of America

OCIS codes: 350.6830, 220.4830, 000.6850, 190.4870, 160.6060.

1. INTRODUCTION

Thermal diffusion, or the Ludwig–Soret effect, is matter flow driven by thermal gradients. In fluid mixtures, it amounts to preferential diffusion of each component along or against ∇T, while in macromolecular solutions or colloidal suspensions, where it is generally known as thermophoresis, it consists of thermally driven migration of suspended particles. Both effects lead, in the absence of convection, to steady-state concentration gradients.[1] Thermal diffusion is therefore a cross-flow effect, coupling heat and mass transfer, phenomenologically described by nonequilibrium thermodynamics. The mass flux J_m of a solute with average concentration $\bar{c}$ in the presence of thermal diffusion can be written as[2]

$$J_m = -D\nabla c - \bar{c}(1-\bar{c})D_T\nabla T, \tag{1}$$

where D is the mass-diffusion coefficient, and D_T is called the coefficient of thermal diffusion. The ratio of thermal to "ordinary" diffusion is called the Soret coefficient,

$$S_T = \frac{D_T}{D} = -\frac{1}{\bar{c}(1-\bar{c})}\frac{\mathrm{d}c}{\mathrm{d}T}. \tag{2}$$

The Soret effect totally lacks so far any microscopic interpretation. For instance, in most cases, the denser component of a binary mixture diffuses toward the cold, showing what is conventionally called a *positive* Soret effect. Yet, examples of negative Soret coefficients are common, and no model can hitherto predict the direction of thermodiffusive motion for a given solute.

The Soret effect has a dramatic effect on convective mixing. Convection in simple fluids heated from below is hampered by viscous friction and thermal conductivity, which quench local density fluctuations and lead to a finite threshold for Rayleigh–Benard convection. In mixtures, conversely, inverted concentration gradients set by thermal diffusion can relax only by mass diffusion, which is far slower than heat transport: hence the convection threshold is dramatically lowered. For a negative Soret coefficient, it is even possible to induce convection by heating from above.[3] Therefore thermal diffusion plays a crucial role in many naturally occurring convective processes, from thermohaline convection in oceans[4] to component segregation in solidifying metallic alloys,[5] volcanic lava,[6] or even in the Earth's mantle.[7] It is also supposed to play an important role in crystal growth.[8] More recently, it has been shown that thermal diffusion sets the scene for giant fluctuations in nonisothermal mixtures.[9]

Thermal diffusion of colloids or macromolecules is an even stronger effect: For instance, recent experiments on DNA solutions[10] have shown that polymer thermophoresis leads to convective patterns where the local macromolecular concentration may be amplified up to a thousandfold, suggesting a possible role of thermophoresis in prebiotic conditions. Studies of thermal diffusion in complex fluids may provide important information on the microscopic origin of the Soret effect. At variance with mass flow in concentrated solutions, particle redistribution in dilute suspensions has little effect on local thermal properties, so that colloids may be thought of as moving in a fixed "thermally inhomogeneous scene" set by the solvent. Moreover, effective forces between colloidal particles can be easily "tuned" by changing the solvent composition, allowing for an extensive survey of thermophoretic effects. Recent measurements of the Soret effect in micellar and protein solutions[11,12] have indeed provided quantitative understanding of electrostatic and solvation effects on thermophoresis.

A serious problem hampering studies of thermophoresis in colloidal fluids is, however, the extremely low value of D, setting the time scale for reaching steady state. For instance, one of the simplest methods for investigating Soret effects exploits the deflection of a laser beam due to the concentration, and therefore the refractive-index gradient, induced by the imposed temperature field.[13] A small temperature difference is rapidly set between two initially isothermal plates by cooling from the bottom and is then kept fixed up to several hours. Passing through the plate gap, the beam undergoes a first rapid downward deflection due to the temperature dependence of the solvent refractive index, followed by a much slower one due to thermal diffusion, eventually leading to steady state.

0740-3224/2004/030605-12$15.00

The Soret coefficient can be directly evaluated from the ratio of these two angular displacements. Yet, imposing thermal gradients between thermally conductive surfaces less than a few hundreds of micrometers apart is hardly feasible, and this makes beam-deflection measurements of the Soret effect in macromolecular fluids time consuming. For instance, the typical time scale to attain steady state for aqueous suspensions of particles with a 10-nm radius, giving a diffusion coefficient $D \approx 2 \times 10^{-7}$ $\mathrm{cm^2\,s^{-1}}$, with plate separation $d = 1$ mm, is of the order of a few times $\tau = d^2/\pi^2 D \approx 5000$ s.

All-optical methods, where laser beams are used in concert for heating up the sample and detecting concentration gradients driven by the Soret effect, allow overcoming of mechanical problems in setting thermal gradients on very small spatial scales. This goal has, for instance, been attained using forced Rayleigh scattering, where two crossing laser beams exploit light absorption by a solubilized dye for "writing" a temperature grating in the sample.[14] Thermal diffusion induces then a concentration, and therefore a refractive-index gradient, acting as a diffraction grating for a weaker probing beam. One of the main advantages of this method is that diffusion spatial scales can be easily changed by varying the crossing angle of the pumping beams. Forced Rayleigh scattering requires, however, elaborate optical setups, powerful laser sources, and very delicate alignment procedures. Furthermore, in order to deal with simple two-dimensional (2-D) gratings, and to avoid taking into account more complex Raman–Nath diffraction effects, measuring cells must have a very short optical path, generally yielding small signals.

We shall try to show that accurate Soret-effect measurements can be performed using thermal lensing, an all-optical technique requiring a much simpler setup. Moreover, the method we propose is specifically designed for working with aqueous solutions, which are systems of foremost interest. At variance with all methods proposed so far, this technique does not perturb the sample by calling for the addition of any light-absorbing molecule.

2. DESCRIPTION OF THE METHOD

A. Thermal-Lensing Effect

Thermal lensing (TL) is a self-effect on beam propagation taking place when a focused laser beam heats up a partially absorbing medium, generating a locally inhomogeneous refractive-index profile.[15,16] Thermal expansion indeed induces a local-density distribution in the sample that, for Gaussian ($\mathrm{TEM_{00}}$) beams, has a simple parabolic shape near the beam center. Such a radial density gradient produces likewise a quadratic refractive-index profile, acting as a negative lens that increases the divergence of the transmitted beam. Beam widening can be accurately measured by detecting even minute changes of the central-beam intensity, making TL suitable for absorption measurements in simple fluids with extinction coefficients as low as 10^{-7}. For this reason, TL has been established as a highly sensitive technique for trace analysis in chromatography and electrophoresis, both in its basic configuration and in more sophisticated instrumentation designs including double-beam, differential, spectrally tunable setups.[17,18]

Besides its excellent performance as a spectroscopic method, TL can be profitably exploited for investigating the Soret effect. In fluid mixtures or solutions, indeed, the laser-induced temperature profile drives Soret motion, leading to the progressive buildup of a concentration gradient within the heated region, which acts as an additional lenslike element. This "Soret lens" can be divergent or convergent, depending on the preferential direction of motion of the component having the largest index of refraction, and as a result, spreading of the transmitted beam may further increase, or conversely lessen. In disperse systems, for instance, if the particles have both a refractive index and a density larger than the solvent, thermophoresis leads to a larger or a smaller beam spreading, depending on whether the Soret coefficient is positive or negative. Due to the different order of magnitudes of thermal diffusivity and mass diffusion, "thermal" and "Soret" lensing effects take place on widely separated time scales, allowing for a precise measurement of the induced concentration gradient and therefore of the Soret coefficient. The first application of thermal lensing to thermal diffusion was made back in 1974 by Giglio and Vendramini, who measured the Soret coefficient in critical aniline/cyclohexane mixtures.[19] Since aniline strongly absorbs in the visible range, and the Soret effect diverges near a critical point,[20] a mildly focused, low-power He–Ne laser induces a beam divergence far exceeding thermal lensing of the pure components. This seminal experiment shows that thermal lensing can be regarded as an all-optical technique combining accuracy in setting localized thermal gradients to experimental simplicity. Recently, TL methods (z scan) for measuring Soret effects have been revived by Alves *et al.*,[21] who also showed preliminary applications to strongly absorbing ferrofluids.

However, water is highly transparent through all the visible range, while its strong infrared absorption starts only for wavelengths beyond 1.2 μm. Therefore visible lasers cannot be used to investigate aqueous suspensions, constituting by far the most interesting class of complex fluids, unless absorbing dyes are added to enhance TL effects. However, extreme attention must be paid to possible preferential adsorption of the dye to the particle surface, which can severely influence the measurement. Moreover, dyes are often present in solution as dissociated ions, limiting therefore the lower value for the ionic strength that can be attained. We notice in passing that the addition of surfactants has often been used as a way to "enhance" thermal-lensing efficiency of pure water: only very recently has this effect been correctly ascribed to thermal diffusion of the surfactant micelles.[22] The main aim of this paper is to show that large TL effects can be obtained in aqueous solutions without introducing any photosensitive probe, and still retain the convenience of working in a spectral region allowing for detection with a simple photodiode. The method we propose exploits water absorption due to a specific vibrational overtone, peaked at $\lambda = 980$ nm (a frequency-doubled combination of the H_2O bending mode with asymmetric stretching) and yields an absorption coefficient $b \approx 0.5\,\mathrm{cm^{-1}}$, which is more than sufficient for obtaining large TL signals.

We regard this choice as very convenient, first, because semiconductor lasers, exactly matching this water absorption peak, are readily commercially available at relatively low cost, since they are largely used in photonics as pump modules for erbium-doped fiber amplifiers. Moreover, being a vibrational band, absorption at 980 nm is very sensitive to isotope substitution: for pure D_2O, indeed, the absorption coefficient decreases to $b \approx 0.08\,\mathrm{cm}^{-1}$. As we shall see, accurate tuning of the solvent thermal-lensing effect is therefore possible by mixing water with D_2O in variable ratios. We point out that heating of aqueous samples can also be obtained by IR lasers operating at $\lambda \cong 1.5\,\mu$m, which are efficiently made to induce the convection patterns observed in Ref. 10. However, the water absorption coefficient in this wavelength range is so high ($b > 20\,\mathrm{cm}^{-1}$) that strongly nonlinear absorption profiles are obtained unless extremely thin samples are used. In addition, while at $\lambda = 980$ nm full monitoring of the beam profile can be obtained by using common CCD cameras, more-expensive IR-enhanced sensors are needed in the farther infrared.

B. Theory

We first recall the basic theoretical results concerning TL in simple fluids. Evaluation of TL effects induced by a Gaussian laser beam of optical power P, incident on a sample with absorption coefficient b, thermal conductivity κ, and thermal diffusivity χ, amounts, first, to solving the heat equation for the local temperature increase $\Delta T(r, t)$,

$$\frac{\partial(\Delta T(r, t))}{\partial t} = \frac{\chi \dot{Q}}{\kappa} + \chi \nabla^2(\Delta T(r, t)), \tag{3}$$

with a source term $\dot{Q}$ given by

$$\dot{Q} = \frac{2Pl}{\pi w^2} \exp\left(-\frac{2r^2}{w^2}\right), \tag{4}$$

where w is the focused beam spot size, l is the optical path in the medium, and r is the distance from the optical axis. The analysis is very much simplified by assuming a 2-D infinite geometry, neglecting heat flow along the optical axis, and then calculating self-effects on beam propagation in the paraxial approximation. Within this simple approximation, Gordon and Whinnery[15] have shown that, in the proximity of the optical axis, $\Delta T(r, t)$ can be written as

$$\Delta T(r, t) = \frac{Pb}{4\pi\kappa}\left[C(t; \tau_{\mathrm{th}}) - \varphi(t; \tau_{\mathrm{th}})\frac{2r^2}{w^2}\right], \tag{5}$$

where $\varphi(t; \tau_{\mathrm{th}}) = (1 + \tau_{\mathrm{th}}/2t)^{-1}$, $C(t) = \ln[1 - \varphi(t; \tau_{\mathrm{th}})]^{-1}$, and $\tau_{\mathrm{th}} = w^2/4\chi$ is the heat diffusion time over the beam spot size. Due to thermal expansion, Eq. (5) leads to a parabolic refractive-index profile,

$$n(0, t) - n(r, t) = \frac{Pb}{2\kappa}\frac{\partial n}{\partial T}\varphi(t; \tau_{\mathrm{th}})\frac{r^2}{\pi w^2}, \tag{6}$$

so that the sample acts as a diverging lens with inverse focal length

$$\frac{1}{f_{\mathrm{th}}} = -\vartheta_{\mathrm{th}}\frac{\lambda}{\pi w^2}\varphi(t; \tau_{\mathrm{th}}), \tag{7}$$

where the dimensionless "thermal-lens number" ϑ_{th} is given by

$$\vartheta_{\mathrm{th}} = -\frac{Pbl}{\kappa\lambda}\frac{\partial n}{\partial T}. \tag{8}$$

As we shall see in what follows, it is particularly useful to give an expression for the fractional reduction, due to the increase of the beam-spreading parameter, of the intensity on the optical axis. To first order in ϑ_{th}, this is given, at steady state, by

$$\frac{\Delta I}{I} \equiv \frac{I(0) - I(\infty)}{I(\infty)} = -\vartheta_{\mathrm{th}}\frac{2\tilde{z}}{1 + \tilde{z}^2}, \tag{9}$$

where $\tilde{z} = z_0/z_R$ is the distance z_0 from the cell to the waist rescaled to the Rayleigh range. As we see, to first order in ϑ_{th}, the TL effect vanishes if the cell is placed exactly at the beam waist, while the effect is maximized by placing the cell at z_R from the beam waist, where the radius of curvature of the incident Gaussian beam is minimal.

A Fresnel diffraction analysis,[23] fully taking into account lens aberrations, leads, however (still to first order in ϑ_{th}), to the slightly more complicated expression for the intensity change at steady state,

$$\frac{\Delta I}{I} = -1 + \left[1 - \vartheta_{\mathrm{th}}\arctan\left(\frac{2\tilde{z}}{3 + \tilde{z}^2}\right)\right]^{-1}, \tag{10}$$

with a full temporal dependence given by $I(t) - I(0) = -I(0)\vartheta_{\mathrm{th}} f(t; \tau_{\mathrm{th}}; \tilde{z})$, where

$$f(t; \tau_{\mathrm{th}}; \tilde{z}) = \arctan\left[\frac{2\tilde{z}}{3 + \tilde{z}^2 + (9 + \tilde{z}^2)\tau_{\mathrm{th}}/2t}\right]. \tag{11}$$

Equation (10) bears an experimentally important difference compared with Eq. (9): the maximal effect is indeed found when the sample is placed not at z_R, but rather at $\sqrt{3}z_R$, from the beam waist. Moreover, the time dependence of the intensity in Eq. (11) becomes explicitly dependent on $\tilde{z}$.

Numerical three-dimensional (3-D) results allowing for axial heat transfer in thick samples,[24] besides removing the spurious logarithmic divergence of $\Delta T(0, t)$ in Eq. (5), which is a consequence of considering an infinite 2-D medium, yield, moreover, axially varying temperature profiles. In addition, as we shall see, the maximal temperature increase on the optical axis becomes a decreasing function of the beam-spot size.

We shall now focus on TL effects in fluid mixtures, trying to show that the previous analysis can be easily extended to thermal-diffusion studies. As a bonus, we shall see that the nature of the specific approximations made, although crucial for thermal-lens spectroscopy, is less relevant to Soret-effect measurements, which are intrinsically differential. The additional thermal-diffusion contribution to the lensing effect can be calculated as follows. Inserting expression (1) into the continuity equation for the mass flow, and using Eq. (2), we have

$$\frac{\partial(\Delta c(r,\,t))}{\partial t} = D\nabla^2(\Delta c(r,\,t)) + S_T\bar{c}(1-\bar{c})\nabla^2(\Delta T(r,\,t)). \tag{12}$$

Since the characteristic diffusion time over the beam-spot size $\tau_D = w^2/4D \gg \tau_{\rm th}$ (in colloidal dispersions or macromolecular solutions, the Lewis number, $L = D/\chi$, is typically smaller than 10^{-4}), for $t \gg \tau_{\rm th}$, we can substitute $\nabla^2(\Delta T(r,\,t))$ from the stationary solution of Eq. (3) as $\nabla^2(\Delta T(r,\,t)) \simeq -\dot{Q}/\kappa$, obtaining

$$\frac{\partial(\Delta c(r,\,t))}{\partial t} = D\nabla^2(\Delta c(r,\,t)) - \frac{S_T\bar{c}(1-\bar{c})D\dot{Q}}{\kappa}, \tag{13}$$

which is formally identical to Eq. (3). Within the same approximation used to obtain Eq. (5), we get, for instance,

$$\Delta c(r,\,t) = -\frac{PbS_T\bar{c}(1-\bar{c})}{4\pi\kappa}\left[C(t;\,\tau_D) - \varphi(t;\,\tau_D)\frac{2r^2}{w^2}\right], \tag{14}$$

where $\varphi(t;\,\tau_D) = (1 + \tau_D/2t)^{-1}$ and $C(t) = \ln[1 - \varphi(t;\,\tau_D)]^{-1}$. This concentration profile acts as a Soret lens having a focal length

$$\frac{1}{f_{\rm S}} = -\vartheta_{\rm S}\frac{\lambda}{\pi w^2}\varphi(t,\,\tau_D), \tag{15}$$

where the dimensionless Soret-lens number $\vartheta_{\rm S}$ is given by

$$\vartheta_{\rm S} = \frac{Pbl}{\kappa\lambda}\frac{\partial n}{\partial c}S_T\bar{c}(1-\bar{c}). \tag{16}$$

Therefore the sample acts as a combined time-dependent lens with total reciprocal focal length $f^{-1} = -(\lambda/\pi w^2)\vartheta$, where

$$\vartheta = \frac{Pbl}{\kappa\lambda}\left[\frac{\partial n}{\partial T}\varphi(t;\,\tau_{\rm th}) - S_T\bar{c}(1-\bar{c})\frac{\partial n}{\partial c}\varphi(t;\,\tau_D)\right]. \tag{17}$$

Since $\tau_D \gg \tau_{\rm th}$, time-scale separation allows evaluation of the Soret coefficient from the ratio of the Soret and thermal-lens numbers as

$$\frac{\vartheta_{\rm S}}{\vartheta_{\rm th}} = -S_T\bar{c}(1-\bar{c})\frac{\partial n/\partial c}{\partial n/\partial T}, \tag{18}$$

which, for $\vartheta_{\rm S},\ \vartheta_{\rm th} \ll 1$, yields

$$\frac{\Delta I_{\rm S+th}}{\Delta I_{\rm th}} = 1 - S_T\bar{c}(1-\bar{c})\frac{\partial n/\partial c}{\partial n/\partial T}, \tag{19}$$

where $\Delta I_{\rm S+th}$ and $\Delta I_{\rm th}$ are the changes in the central-beam intensity for $t \gg \tau_D$ and $\tau_{\rm th} \ll t \ll \tau_D$, respectively. Due to the identity of the governing equations for thermal and Soret lensing, expression (18) holds independently of the approximations made, so that S_T can be directly calculated once the material parameters $\partial n/\partial c$, $\partial n/\partial T$ are known, and the intensity change solely due to the thermal effect is measured. Within the (aberrant lens) 2-D approximation, the time dependence of the Soret lens will be given by $f(t;\,\tau_D;\,\tilde{z})$, so that D can be obtained from a fit of the temporal buildup of the Soret lens (more technically, D is the long-time collective diffusion coefficient). In addition, as already noticed in Ref. 13, methods for extracting D from Soret measurements are much less affected by spurious dust effects than dynamic light scattering.

C. Convection Effects

Since radially symmetric beams necessarily generate horizontal temperature gradients, free convection is *unavoidably* present in TL measurements, regardless of the chosen experimental configuration. It is therefore curious that little attention has so far been paid to convective effects on thermal-lensing experiments, if exception is made of earlier treatments of self-action of laser beams.[25] There, however, a finite threshold for the onset of convection, based on a simple Rayleigh–Benard criterium applied to the beam-induced inverted *vertical* temperature profile, was assumed: Conversely, horizontal gradients will induce a finite convection velocity U for *any* value of the incident power.

For what concerns thermal lensing in simple fluids, the question is, therefore, whether convective motion sensibly disturbs the beam-induced temperature profile. When inertial forces are negligible, a characteristic value $\tilde{U}$ for the convection velocity is found by equating viscous forces to buoyancy as

$$\tilde{U} \sim g\alpha_0\ell_g^2\Delta T/\nu, \tag{20}$$

where ν is the kinematic viscosity, ℓ_g is the vertical length over which buoyancy acts, and α_0 is the thermal-expansion coefficient (for water, $\alpha_0 \simeq 2 \times 10^{-4}\,{\rm K}^{-1}$). Disturbance of the temperature profile will therefore be negligible, provided that, on the beam-spot length scale, heat diffusion is much faster than convection, which happens whenever $\tau_{\rm th} \ll w/\tilde{U}$, or

$$w\ell_g^2 \ll \frac{4\nu\chi}{g\alpha_0\Delta T}. \tag{21}$$

As we shall see discussing numerical simulations, in normal experimental conditions, where $\tau_{\rm th} \sim 10^{-3}\,{\rm s}$, this condition is easily fulfilled, leading to the important consequence that the thermal profile remains essentially unchanged even in presence of consistent convection.

The concentration profile associated with thermal diffusion, however, sets in on the much longer time scale $\tau_D = w^2/4D$, which for large colloidal particles may range up to tens of seconds, so that Eq. (20) is substituted by the much more stringent condition

$$w\ell_g^2 \ll \frac{4\nu D}{g\alpha\Delta T}, \tag{22}$$

where, using Eq. (2), the total thermal-expansion coefficient α, which includes an additional contribution from solute thermal diffusion and thermal expansivity, can be written as

$$\alpha = \alpha_0 + \beta c(1-c)S_T, \tag{23}$$

where $\beta = \rho^{-1}(d\rho/dc)$, and ρ is the density of the solution. As we shall see, this makes consideration of convective effects on TL Soret measurements crucial. Equation (21) allows for discussion of the effectiveness of different

experimental configurations. As is obvious, convective effects can be limited by reducing the beam-spot size, since diffusion dominates over small spatial scales. We recall, however, that, at variance with the 2-D result, full 3-D treatments show that, at constant power, the temperature increase on the optical axis is larger for smaller w. In addition, it should be noticed that z_R decreases as w_0^2, therefore limiting the maximum useful optical path l: in practice, even using cells with l as small as 100 μm, w_0 cannot be smaller than 15 μm. The whole apparatus can then be set either horizontally or in an upright position with the vertical optical axis. In the former case, the buoyancy length scale ℓ_g coincides for cylindrical cells with the cell radius, which can be harder to make smaller than a few millimeters. The upright configuration presents a crucial advantage, since ℓ_g coincides in this case with l, which can easily be made much smaller, obviously at the price of a smaller signal. However, since the maximum input power allowing Eq. (21) to be satisfied scales as l^{-2}, the maximum useful beam widening scales as $\vartheta_{\max} \sim P_{\max} l \sim l^{-1}$, so that reducing the cell vertical thickness still allows larger TL signals to be obtained.

It is finally useful to discuss whether the radiation pressure of the incident beam, which yields a net force per unit volume $F_r \simeq Ib/c_0$, where c_0 is the speed of light, may independently contribute to convection. In our typical experimental conditions, the ratio of radiation to buoyancy forces per unit volume, $F_r/F_b \sim \kappa/(w_0^2 c_0 \rho g \alpha)$, which does not depend therefore on P or l, turns out to be only of the order of 0.1–0.15. This additional effect therefore, although nonnegligible, is modest, and will be neglected in what follows. However, we point out that radiation-pressure induced convection may be dominant for experiments performed using tightly focused beams.

3. NUMERICAL SIMULATIONS

A. Outlines of the Method

We have performed numerical simulations of the thermal disturbance and of the associated optical lensing properties induced in aqueous macromolecular solutions by the absorption of a focused Gaussian beam. Although convection in binary mixtures is a delicate hydrodynamic problem, dedicated numerical routines, allowing for fast and accurate solution of the coupled Navier–Stokes, heat-transport, and mass-diffusion equations, are presently available. To solve simultaneously the optical diffraction problem and also to get better insight of the physical aspects of the numerical solutions, we rather choose to use a more general finite-elements solving routine, Flex PDE 3.03 Professional (Pde Solutions Inc., USA), requiring a direct implementation of the governing equations and of the solving grid. By exploiting the cylindrical symmetry of the problem, we have chosen a 2-D self-adapting mesh of ~10,000 triangular elements, forcing, however, the mesh size to be sensibly smaller in the proximity of the optical axis, to achieve better accuracy in the region where larger gradients are expected. For what concerns temperature profiles and flow pattern, the simulation results were checked using a "standard" finite-elements routine for fluid dynamics, Fluent 6.0 (Fluent Inc., USA), with an uniform grid of ~50,000 rectangular cells. The latter routine was also used for problems specifically requiring a 3-D simulation, using uniform mesh of ~50,000 hexahedric cells.

A specific technical point worth noticing concerns the pressure field $p(\mathbf{r})$, which is needed for solving the Navier–Stokes equation, but is not immediately given an equivalent of the momentum equation: as is well known in computational fluid dynamics, this often poses serious problems in setting suitable border conditions. We have chosen using the so-called "Poisson pressure" or "modified continuity" method, which amounts to solving an equation for $p(\mathbf{r})$, ensuring consistence with the original Navier–Stokes equation.[26] The pressure equation is obtained by taking the divergence of the momentum equation and using the incompressibility condition, getting

$$\nabla \cdot \nabla(p/\rho) = \nabla \cdot \mathbf{f} - \nabla \cdot (\mathbf{U} \cdot \nabla)\mathbf{U}, \tag{24}$$

where $\mathbf{f}$ is the external force per unit volume. Since this equation follows directly from the solenoidal character of the velocity field, but does not conversely *imply* it, it is, however, essentially enforcing incompressibility by adding to the Poisson pressure equation the condition $\nabla \cdot \mathbf{U} = 0$, weighted by an appropriate penalty coefficient δ, finally obtaining

$$\nabla \cdot \nabla(p/\rho) = \nabla \cdot \mathbf{f} - \nabla \cdot (\mathbf{U} \cdot \nabla)\mathbf{U} + \delta \nabla \cdot \mathbf{U}, \tag{25}$$

where δ is tuned to ensure simultaneously accuracy and convergence of the algorithm. This approach leads to a natural boundary condition for the pressure $\mathbf{n} \cdot \nabla(p/\rho) = 0$ on the cell contour.

As a first example of numerical results, we shall discuss the dependence of the central-beam intensity on the cell position with respect to the beam waist, neglecting, for the moment, convective effects (which can be simply obtained by setting to zero the buoyancy term). As shown in Ref. 24, heat transport along the optical axis may sensibly modify the beam-induced temperature profile: we have compared the 2-D analytical result (10) with the full numerical solution, obtained using the Wu and Dovichi 3-D analysis[24] and calculating beam propagation from the Fresnel diffraction approach presented in Ref. 23. Far-field intensity changes have been evaluated for absorption of 980-nm radiation by water at 20 °C ($b = 0.5\,\mathrm{cm}^{-1}$, $\kappa = 0.61\,\mathrm{W m}^{-1}\,\mathrm{K}^{-1}$, $\chi = 1.44 \times 10^{-3}\,\mathrm{cm}^2\,\mathrm{s}^{-1}$) in a vertical optical axis configuration, imposing $\Delta T = 0$ on the lateral walls, while the boundary condition on the top and bottom optical glass windows is $\partial(\Delta T)/\partial z = (-\kappa_{\mathrm{win}}/\kappa l_{\mathrm{win}})\Delta T$, where l_{win} and κ_{win} are the window thickness and thermal conductivity. To simulate cells having an optical path that is not negligible compared with z_R, we have also taken into account, at variance with Ref. 24, the spread of the beam during propagation in the cell. Figure 1, which displays results obtained by varying P and l, but keeping Pl constant, first shows that, using glass windows with low thermal conductivity, the effects of axial heat transport are in general modest. The nonmonotonic dependence on l stems from two conflicting effects. Increasing l leads to an increase of the average ΔT in the cell, due to a minor relevance of axial heat losses: yet, when l is a sizeable fraction of z_R, the beam curvature is not everywhere optimal, causing a decrease of TL efficiency.

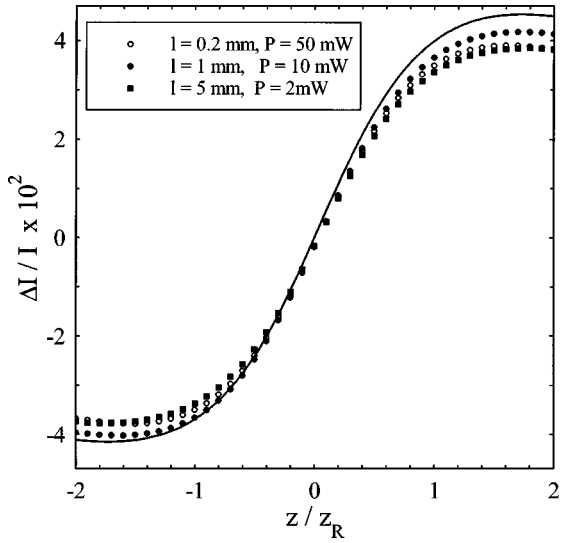

Fig. 1. Fractional change of the central-beam intensity as a function of the distance z from the cell entrance window to the beam waist, calculated according to the text for different values of P and l, but constant Pl, compared with the analytical 2-D expression (10) (solid curve).

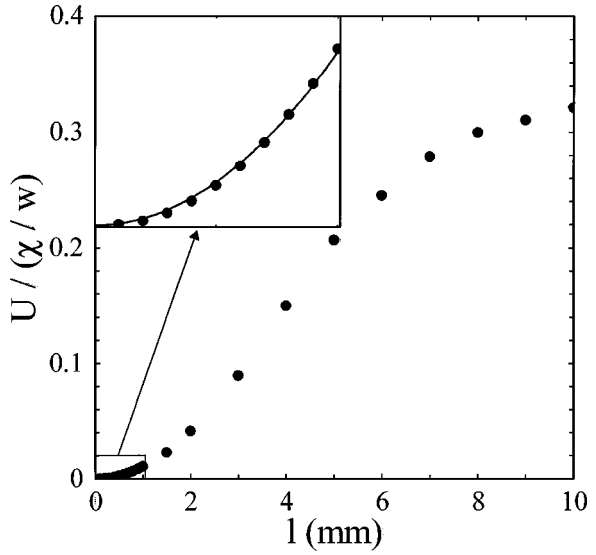

Fig. 2. Numerical results for the convection velocity at the center of the cell, normalized to χ/w, as a function of the cell thickness, for $w_0 = 60\,\mu$m, $P = 20$ mW. Values obtained for $l \leq 1$ mm are fitted with a parabola in the inset.

B. Thermal Profiles in the Presence of Convection

We shall first inquire whether the scaling behavior of the expression (19) holds, in particular, for what affects the dependence of the convective fluid velocity U on the cell thickness l. Numerical results for U in the upright cell configuration, evaluated at the cell center, and made dimensionless by scaling to $\chi/w = 0.12$ cm/s, are shown in Fig. 2. The plot shows that the predicted quadratic increase of U with l holds for sufficiently small convection velocity. However, the values of the convective velocity obtained by using either Flex PDE or Fluent are more than one order of magnitude smaller than $\tilde{U}$: Equation (19) yields therefore a correct scaling, but grossly overestimates the absolute value of U. By increasing the vertical cell thickness, the rate of velocity increase gets far smaller. The dimensional argument leading to Eq. (19) is indeed valid only at low Grashof number $\mathrm{Gr} = g\alpha\Delta T l^3/\nu^2$, while in the opposite limit of high Gr, equating this time buoyancy to inertia forces, $\tilde{U}$ may be expected to scale as $\tilde{U} \sim \sqrt{g\alpha\nu l\Delta T}$, and therefore to increase only as the square root of the cell thickness.

A comparison of the full convection patterns obtained both in the upright and in the horizontal cell configurations, for the same values of the incident power $P = 20$ mW and minimal beam spot size $w_0 = 45\,\mu$ms (so that, at $z = \sqrt{3}z_R$, $w \simeq 90\,\mu$m), is shown in Fig. 3. Both patterns show two counterrotating convection rolls, mostly confined in the central region of the cell: confinement of the rolls in a layer that is sensibly smaller than the cell vertical thickness reduces ℓ_g, and therefore leads to smaller values of $\tilde{U}$. However, the most striking feature of the patterns is that convection velocities in the upright configuration are almost two order of magnitudes smaller than in the horizontal configuration, which is in good agreement with the scaling of U with ℓ_g^2. Theoretical arguments and numerical simulation fully agree, therefore, about the convenience of adopting an upright configuration of the TL apparatus.

For TL measurements in pure fluids, the experimentally relevant question is how much convective patterns influence the thermal, and therefore refractive-index, profile. Figure 4 displays the numerical results for the steady-state temperature profiles in a water-filled cell, having optical path $l = 0.5$ mm and placed in upright configuration at $\sqrt{3}z_R$ from the beam waist ($w_0 = 45\,\mu$m), for increasing values of the incident power. The plot shows that the profiles obtained in the absence of convection (forcing $g = 0$) and for $P = 0.5$ W (which is, as

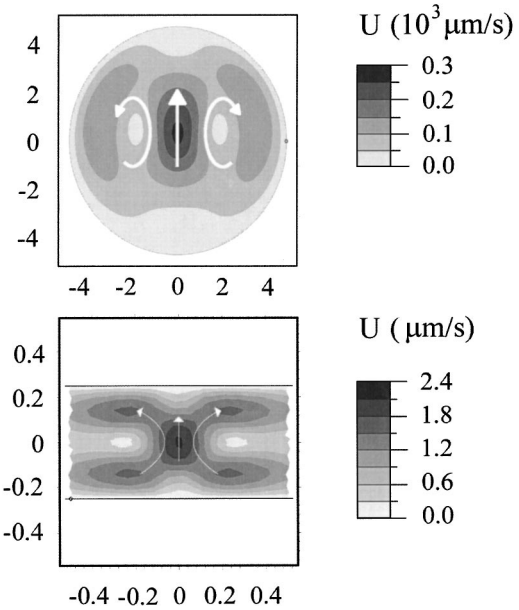

Fig. 3. Thermal convection patterns in a cylindrical cell of diameter $d = 9$ mm and optical path length $l = 0.5$ mm, in horizontal (top) and upright (bottom) optical axis configurations, with axes units in millimeters. Arrows indicate the flow direction in the convective rolls.

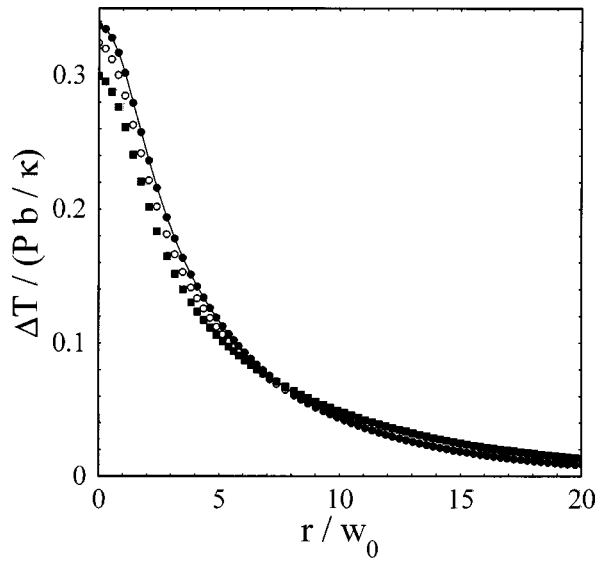

Fig. 4. Numerical results for the temperature profile in a cylindrical cell of diameter $d = 9$ mm and optical path length $l = 0.5$ mm, in an upright optical axis configuration, for an incident beam power of 0.5 (●), 10 (○), and 20 (■) W, focused to a minimal spot size $w_0 = 45\ \mu$m. The solid curve is the thermal profile in the absence of convective motion.

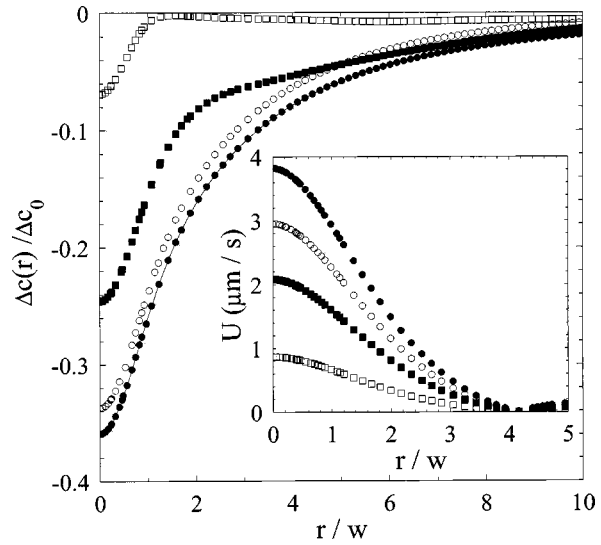

Fig. 5. Main body: Numerical results for concentration profiles, normalized to $\Delta c_0 \equiv S_T c(1-c)Pb/\kappa$, obtained for ξ=0.01 (●), 0.1 (○), 1 (□), and 10 (■). The solid curve is the profile in the absence of convection. Inset: Velocity profiles for a solute with β=0.15 and $S_T = +0.02\,\mathrm{K}^{-1}$ (●) or $-0.02\ \mathrm{K}^{-1}$ (□). Open symbols refer to simulations made for β=0 (○) and $\alpha_0 = 0$ (□).

we shall see, much higher than the typical power used in the measurements) are identical. Since, for $P = 0.5$ W, $U \simeq 70\ \mu\mathrm{m\ s}^{-1}$ at the cell center, $wU/4\chi \simeq 0.01$; this result is consistent with the approximate criterium (20). Slight changes in the temperature profile can indeed be noticed only for $P = 10$ W (corresponding to $wU/4\chi \simeq 0.2$) and become consistent for $P = 20$ W, where also the velocity pattern in the cell is considerably modified.

C. Concentration Profiles in the Presence of Convection

As we have previously noticed, due to the small value of the Lewis number, convection may be expected to have noticeable effects on concentration profiles when $\tau_D \gtrsim w/U$, that is, when $\xi = wU/4D \gtrsim 1$. We have therefore performed simulations of the concentration profiles for different values of ξ using $\beta = 0.15$, $S_T = 0.02\,\mathrm{K}^{-1}$, which approximately corresponds to the parameter values for the micellar solutions we discuss in the last section. The system configuration is identical to setup used for simulating thermal profiles, and ξ is increased by varying D in the range 10^{-4}–$10^{-7}\,\mathrm{cm^2\,s^{-1}}$, keeping P fixed at 20 mW. The main body of Fig. 5 shows that, while $\Delta c(r)$ fully coincides for $\xi = 0.01$ with the profile obtained in the absence of convection, at $\xi = 0.1$, a modest effect is already evident (we recall that, since S_T is positive, the solute drifts to the cold). For $\xi = 1$, the reduction of the "concentration well" induced by thermophoresis already amounts to 35%, and at $\xi = 10$ the concentration profile is practically destroyed. A reasonable criterium for avoiding relevant errors in thermal-diffusion measurements, which we have used in all the experiments we shall present, is ensuring that $\xi < 0.1$. Particular care should, however, be taken in evaluating U, which is influenced by the Soret coefficient of the solute. The inset in Fig. 5 shows indeed that the total velocity profile is roughly the algebraic sum of the profiles obtained in the absence of thermal diffusion (obtained by setting $\beta = 0$) and for a pure solutal convection in a fictitious solvent with temperature-independent density. Therefore convection effects are stronger for solutes having a large density mismatch with a solvent, yielding a larger value of β. It is also interesting to note that, as already known, thermal diffusion to the hot plate of solutes that are denser than the solvent (so that $S_T < 0$) tends to stabilize the system against convection.

4. SETUP AND CALIBRATION

A. Optical and Mechanical Setup

On the basis of the previous considerations on convective effects, our experimental setup has been configured with an upright optical axis, using a massive rail system vertically placed over an antivibration table. Optical elements, used for collimating the diverging light exiting the fiber-coupled laser and for focusing the beam into the cell, are inserted in precision mechanical carriers and aligned using micrometric translation stages. An overall view of our setup is shown in Fig. 6, while specific components are discussed below.

1. Source

We have used a laser-diode module, LD (Blue Sky Research erbium-doped fiber amplifier 980, USA) operating at 980 nm, with a maximum output power of 120 mW and emission spectral stability ensured by the Bragg-grating structure of the active region. Besides limiting power requirements, efficient coupling to a 2-m-long monomode optical fiber (Corning Flexcore HI1060) ensures a well-characterized spatial beam profile. The fiber ends with a FC connector, inserted in a precision gimbal mounting allowing for accurate fiber positioning. The diode is powered by a precision current driver, *D*, (Newport 505AN, USA), interfaced with a PC, eventually controlling laser operation and output power.

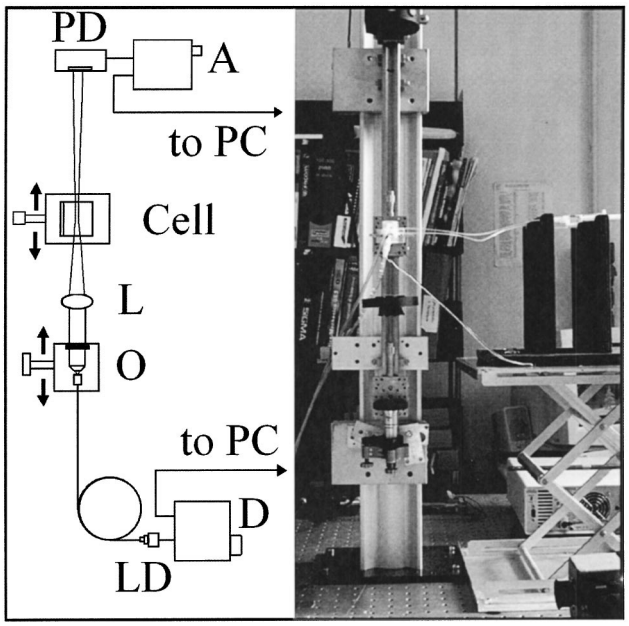

Fig. 6. Layout (left) and picture (right) of the thermal-lensing apparatus in an upright configuration.

2. Optical System

Collimation of the fiber output beam is made using the infinity-corrected objective, O (Leica L-40X, focal length $f_O = 4.55\,\mathrm{mm}$), with numerical aperture NA = 0.66 matched to the fiber, thus ensuring both a good objective filling factor and accurate output wave-front quality. When the fiber is positioned in the objective front focal plane, the output beam is fully collimated with a $1/e$ radius $w_c = 0.42\,\mathrm{mm}$. Fine translation of the collimating objective allows, however, for introducing a mild beam divergence, so as to change the beam radius w_L on the focusing lens and consequently tune the focused spot size. The focusing lens L is a 1-in. Newport Gradium singlet with focal length $f = 80\,\mathrm{mm}$, antireflection coated for the near-infrared spectral range. Gradium lenses, ground from special optical glass having a longitudinal gradient of the refractive index, ensure an almost diffraction-limited spot in the focus and extremely low wave-front distortion. The collimated-output configuration gives a focused spot size $w_0 = f\lambda/\pi w_L \approx 60\,\mu\mathrm{m}$ and a Rayleigh range $z_R \approx 12\,\mathrm{mm}$. By translating O, w_0 can be reduced to 30 μm, corresponding to $z_R \approx 3$ mm.

3. Thermal-Lensing Cells

Since no external thermal gradient has to be imposed, simple spectrometric cuvettes suffice for TL measurements. For the experiments on micellar solutions we shall discuss shortly, which are weakly affected by convection problems but may require accurate thermalization, we use a 5-mm optical-path, 9-mm internal-diameter cylindrical cuvette (Hellma 165-QS), enclosed in a quartz jacket allowing circulation of water from a thermostatic bath. For measurements on suspensions of larger latex particles, simpler nonthermostatted cells with a shorter optical path ($l = 0.5$ and 0.2 mm) are used. Cells are filled using syringes connected to capillary Teflon tubing inserted in the cell stoppers and are fixed on a micrometric unit, allowing for accurate translation along the optical axis required, from Eq. (10), for maximizing TL effects.

4. Signal Detection

According to relation (18), the Soret coefficient can be extracted from a measurement of beam spreading in the far field, for instance, by measuring the full beam profile using a CCD camera. It is, however, faster and easier monitoring the intensity on the optical axis using a photodiode; since the center-beam intensity depends quadratically on the beam size, this detection method, besides allowing for faster data acquisition, is also more sensitive. The photodiode PD we use is placed behind a pinhole selecting less than 0.5% of the beam-spot area and is inserted in a precision XY translator. The signal coming from the sensor is then amplified by a wide-bandwidth amplifier A, sampled at 100 kS/s by an analog-to-digital acquisition board, and eventually elaborated using custom-made software.

B. Calibration

We first show that the experimental setup we have just described allows obtaining strong and reproducible TL effects from water, which are in good agreement with the theory presented in Section 2. The main body of Fig. 7 displays the experimentally measured fractional change in the center-beam intensity $\Delta I/I$ as a function of the reduced distance from the beam waist, obtained in two different experimental conditions. Open dots, which show a maximum value $\Delta I/I \simeq 5\%$ (corresponding to $\vartheta_{\mathrm{th}} \simeq 0.1$, and therefore to an increase in the beam divergence $\vartheta_{\mathrm{th}}\lambda/\pi w \simeq 0.3\,\mathrm{mrad}$), are data obtained at $T = 26\,^{\circ}\mathrm{C}$ for a beam power $P = 50\,\mathrm{mW}$, incident on a water-filled cell with short optical path cell $l = 200\,\mu\mathrm{m}$ (so that $Pl = 10^{-3}\,\mathrm{W\,cm}$). As shown in the plot, in these "weak sig-

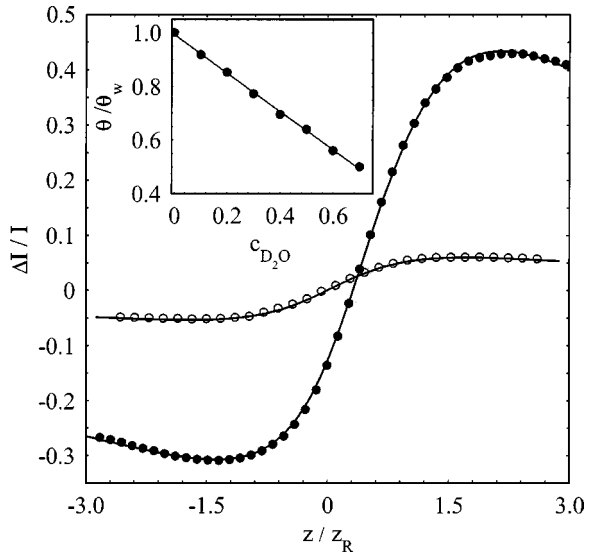

Fig. 7. Measured TL effects in water, as a function of the cell distance from the beam waist, for $P = 50\,\mathrm{mW}$, $l = 0.02\,\mathrm{cm}$, $T = 26\,^{\circ}\mathrm{C}$ (○), and $P = 18\,\mathrm{mW}$, $l = 0.5\,\mathrm{cm}$, $T = 20\,^{\circ}\mathrm{C}$ (●). The solid curves are fits using Eqs. (10) and (26), respectively. Inset: Thermal-lens number for D_2O solutions, normalized to its value ϑ_w for water.

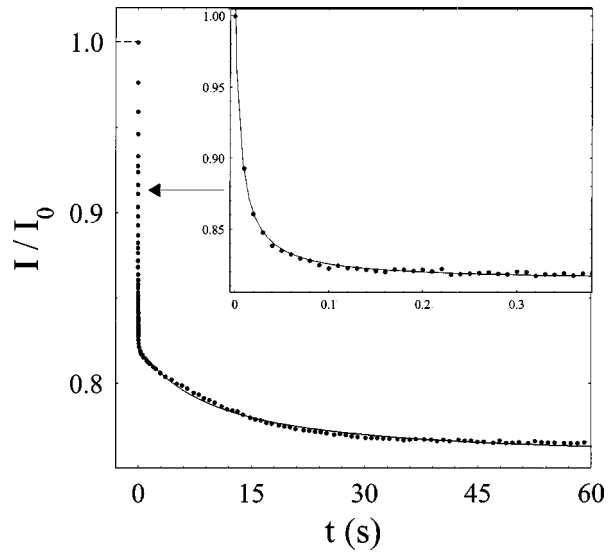

Fig. 8. TL signal for a 25-g/l water solution of sodium dodecyl sulfate in the presence of 20-mM NaCl. The inset shows the buildup of the initial thermal effect, taking place in a very short time. Transients are fitted using the buildup functions $f(t;\ \tau_D;\ \sqrt{3})$ and $f(t;\ \tau_{\mathrm{th}};\ \sqrt{3})$, respectively.

nal" conditions, Eq. (10), using $b = 0.5\,\mathrm{cm}^{-1}$, $\kappa = 0.61\ \mathrm{W\,m^{-1}\,K^{-1}}$, fits the data very well. Since we have not found in the literature accurate values for the temperature dependence of the water refractive index at 980 nm, this quantity was left as the only free parameter in the fit: The best fit value $\mathrm{d}n/\mathrm{d}T = 1.27 \times 10^{-4}\,\mathrm{K}^{-1}$ is anyway quite close to the tabulated value for the visible range $\mathrm{d}n/\mathrm{d}T \simeq 1.1 \times 10^{-4}\,\mathrm{K}^{-1}$. The second set of experimental data (full dots), which has been obtained at $T = 20\,^{\circ}\mathrm{C}$ with lower incident power $P = 18\,\mathrm{mW}$, but using a much longer optical path $l = 5\,\mathrm{mm}$ ($Pl = 10^{-3}\,\mathrm{W\,cm}$), shows fractional intensity changes that can be higher than 30% ($\vartheta_{\mathrm{th}} = 0.7$). A lowest-order expansion is not sufficient to account correctly for such large TL effects, and Eq. (10) has to be modified to include second-order terms in ϑ_{th}, obtaining the more complicated expression[27]

$$\frac{\Delta I}{I} = -1 + \left\{1 - \vartheta_{\mathrm{th}} f(\tilde{z}) + \frac{\vartheta_{\mathrm{th}}^2}{4}[f^2(\tilde{z}) + g^2(\tilde{z})]\right\}^{-1}, \tag{26}$$

where $f(\tilde{z}) = \arctan[2\tilde{z}/(3 + \tilde{z}^2)]$ and $g(\tilde{z}) = (1/2)\ln[(1 + \tilde{z}^2)/(9 + \tilde{z}^2)]$. Using Eq. (25), we obtain $\mathrm{d}n/\mathrm{d}T = 0.91 \times 10^{-4}\,\mathrm{K}^{-1}$, which coincides with the value of $\mathrm{d}n/\mathrm{d}T$ for water at $T = 20\,^{\circ}\mathrm{C}$ in the visible. Finally, the inset shows that the solvent thermal-lens number can be accurately tuned by using D_2O/H_2O mixtures.

As a first example of TL effects associated with thermophoresis, we show in Fig. 8 a typical signal obtained from a micellar solution of sodium dodecyl sulfate (SDS) that we shall further discuss in the next section. The light intensity measured by the photodiode first shows a rapid reduction due to the pure thermal effect, followed by a further, much slower, decrease due to the buildup of the Soret concentration gradient. The solid curve, which is a fit of the time dependence of the Soret TL effect with inequality (11), using $f(t;\ \tau_D;\ \tilde{z} = \sqrt{3})$, yields for the SDS micelles a diffusion coefficient $D = 1.6 \times 10^{-6}\,\mathrm{cm^2\,s^{-1}}$, which is in good agreement with dynamic light-scattering results. Fast photodiode detection and wide separation of time scales also allows analysis of the temporal buildup of the pure thermal lens, which is shown in expanded scale in the inset. Fitting the data by inequality (11), we get $\chi \simeq 2 \times 10^{-3}\,\mathrm{cm^2\,s^{-1}}$, which is in fair agreement with the tabulated value for water thermal diffusivity.

5. APPLICATION TO COMPLEX FLUIDS AND COLLOIDAL SUSPENSIONS

We shall present some applications of the TL setup to systems of interest for soft matter physics, and in particular, to solutions of amphiphilic aggregates and suspensions of spherical colloids. Here, however, we shall not try extracting detailed information on the microscopic nature of thermophoresis from the preliminary measurements we present. Rather, we shall simply regard them as examples of the usefulness of the TL method for obtaining fast and accurate results on thermal diffusion. In the first application, we check that the accuracy of results that can be obtained from TL measurements is comparable to those obtained by the beam-deflection method. Then, we show that TL can be profitably exploited to analyze thermal diffusion in surfactant solutions having very high viscosity, which are difficult to measure using beam deflection due to their very low mass-diffusion coefficient. Finally, we present results obtained on suspensions of silica particles, where the large particle size (tens of nanometers) makes beam-deflection measurements prohibitive, and which also represents an example of a negative Soret coefficient.

A. SDS Micellar Solutions

We choose to repeat some of the measurements performed by Piazza and Guarino[11] on micellar solutions of SDS, a well-known ionic surfactant that in solution forms spherical micelles of radius $R \approx 2.5\,\mathrm{nm}$. Since SDS micelles are charged, they interact through strong electrostatic forces, which strongly modify their thermophoretic behavior. In simple words, since repulsive electrostatic interparticle interactions oppose the buildup of concentration gradients, the Soret coefficient decreases by increasing SDS concentration. Interparticle forces can be tuned by adding salt, which screens electrostatic forces and in addition modifies the single-particle (zero-concentration limit) Soret coefficient. Careful measurements of the concentration dependence of S_T yields important information about interparticle forces, while the zero-concentration limit of S_T is related to particle–solvent interactions.[11] Figure 9 compares the results obtained in Ref. 11 for two values of added salt concentration with those we found using the TL setup, showing that the two sets of values for S_T are very close. To improve data accuracy, S_T was evaluated from a straight-line fit of ϑ versus the laser incident power P, as shown in the inset. In addition, as we anticipated, this method allows checking for possible convection effects. Indeed, when concentration profiles are disturbed by convection, noticeable deviations from the linear behavior are observed, and ϑ tends to saturate for high P.

B. Thermal Diffusion Near a Lyotropic Liquid-Crystal Transition

Triton X100 is a commercial nonionic surfactant, forming in water, at low concentration, spherical micelles with a radius $R \simeq 3$ nm. For surfactant weight fraction exceeding $c^* \simeq 35–40\%$, however, the solution shows a transition to a lyotropic liquid-crystalline phase LC, where very elongated, cylindrical micelles are arranged on a hexagonal lattice. The Soret coefficient is known to diverge near a second-order phase transition[28]: it is therefore interesting to investigate whether there are effects of a first-order transition to a mesogenic phase on thermal diffusion. Unfortunately, concentrated Triton solutions have very high viscosity ν, so that D is very small, implying extremely long duration for beam-deflection measurements. Conversely, the high value of ν, which effectively quenches convection effects, is particularly helpful for TL measurements, which can be performed even using a long optical-path cell with the benefit of a large reduction in measuring time. From the perspective of TL measurements, Triton has a second advantage. Its density $\rho \simeq 1.035$ is indeed quite close to the density of water, so that the solute contribution to convection is particularly small. To reduce further convective effects, we choose to prepare Triton solutions in D_2O/H_2O mixtures, containing ~60% heavy water, which are density matched with the surfactant. The inset in Fig. 10 shows that Triton solutions display very strong TL signals, corresponding to a large Soret-lens number. Therefore to separately account for the intensity changes due to the thermal and the Soret effects, we should use Eq. (25). However, Eq. (18) holds to all orders, so that the Soret coefficient can be simply evaluated by comparing the initial and long-time thermal-lens numbers.

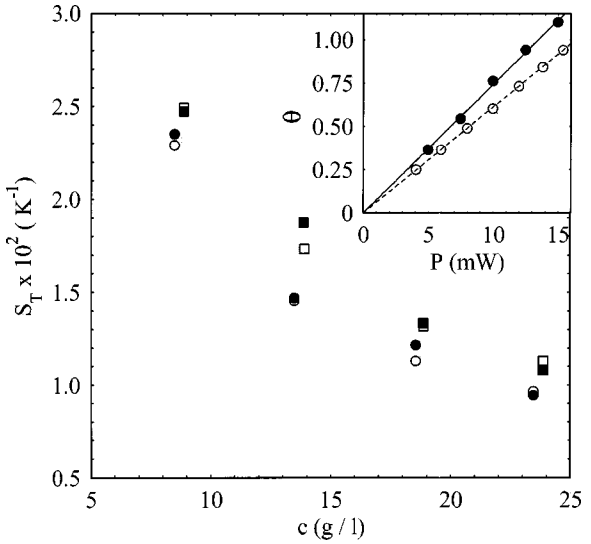

Fig. 9. Soret coefficient of SDS micellar solutions as a function of surfactant concentration, in the presence of 10-mM (circles) and 20-mM (squares) NaCl, using the TL (full symbols) and beam-deflection (open symbols) methods. Inset: Thermal-lens number ϑ versus incident power P for pure water (○) and for a 10-g/l SDS solution (●).

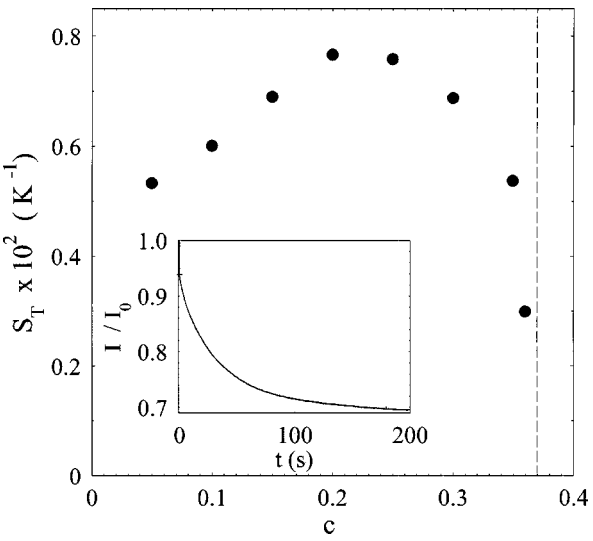

Fig. 10. Inset: TL signal for a $c = 10\%$ Triton X100 solution at room temperature. Main body: Soret coefficient for Triton solutions as a function of surfactant concentration. A vertical broken line is drawn in correspondence to the experimental c^* value for Triton in the 60% D_2O mixture we have used.

The main body of Fig. 10 shows that thermal diffusion displays a distinctive, rather surprising behavior approaching the LC transition. While S_T shows indeed an almost linear growth up to concentrations $c \simeq 20\%$, it decreases rapidly at higher c, suggesting that thermophoretic effects may vanish at c^*. This means that, despite the strong decrease of the mass-diffusion coefficient approaching c^*, the thermal-diffusion coefficient D_T decreases *faster* than D. This behavior is quite different from what has been found for thermal diffusion near a glass transition temperature T_g,[29] where D_T and D vanish with a similar trend, so that S_T does not show any anomaly. We are presently investigating this effect in more detail.

C. Negative Soret Effect in Suspensions of Colloidal Silica

Colloidal particles driven by a thermal gradient to the *hot* side are relatively rare, one of the few examples being proteins, whose direction of thermophoretic motion may be switched by changing temperature.[12] Here we show that this "thermophilic" behavior, corresponding to a negative Soret coefficient, can also be observed for rigid colloidal spheres. Ludox TMA™ is a commercial dispersion (produced by Grace Davison, USA) of colloidal silica nanospheres with radius $R \simeq 11$ nm. At variance with most charged colloidal suspensions (including most of the Ludox™ family), Ludox TMA displays an exceptional stability to salt-induced coagulation. While most latices precipitate or gel by the addition of electrolytes in the millimolar concentration range, Ludox TMA remains in a stable sol phase up to very high ionic strength (by performing dynamic light-scattering measurements, we indeed did not find any evidence of aggregates up to at least 0.5 M of added NaCl). Although the precise reason for this peculiar behavior is not explicitly stated by the producer, this means that colloidal stability is ensured by mechanisms that are not of a simple electrostatic nature. Combination of large particle size and high solute density (for silica, $\rho \cong 1.9$) make Ludox a "test bench" for study-

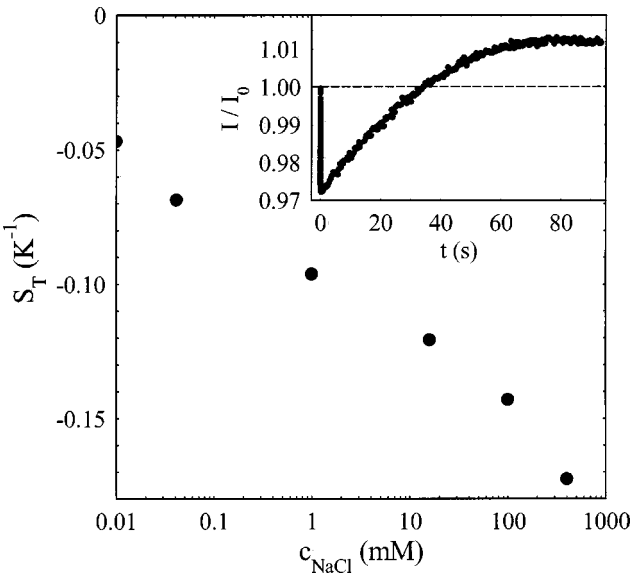

Fig. 11. Inset: Negative TL signal for a $c = 2.5\%$ Ludox TMA suspension. Main body: Soret coefficient for Ludox TMA suspensions as a function of added salt concentration.

ing convection effects on TL measurements: in order to obtain reproducible good-quality signals, we indeed had to use the shortest optical path ($l = 200\ \mu$m) cell, limiting Pl to less than 5×10^{-4} W cm. The absence (or limited effect) of convection is checked both by confirming linearity of ΔI with the input power and by controlling that the signal reaches a stable baseline. The inset in Fig. 11 shows that the Soret TL effect for Ludox solutions has an opposite sign compared with the pure thermal contribution. Moreover, the effect is so large that, even at a Ludox weight fraction as low as 2.5%, the overall beam divergence is *reduced* by passing through the cell, which behaves as a *converging* lens. We have also confirmed that S_T is negative by performing beam-deflection measurements. Due to the large size of Ludox silica colloids, however, the latter required typically as much as 5 h. The main body of Fig. 11 shows that S_T becomes increasingly negative by adding NaCl. Therefore, consistently with what has been found for charged micelles,[11] electrostatic effects, which are stronger at low salt concentration, seem to give a positive contribution to S_T. Although so far we have no explanation for the Soret effect in Ludox, such a large negative value for S_T suggests that, by increasing both particle concentration and the optical path in the cell, and provided that convection effect can be appropriately limited, the Soret self-focusing of the incident beam can be increased to the point that full self-trapping of the beam is obtained.

6. CONCLUSIONS

We have seen that thermal-lensing measurements of the Soret effect in aqueous solutions can be performed using an all-optical method that does not require the addition of photosensitive probes, provided that they are supported by a careful analysis of convective effects. As a final remark, we notice that, due to its simple optical configuration, this apparatus is particularly suitable for measurements in microgravity, where requirements of avoiding buoyancy-driven convection are relaxed, and radiation pressure effects can be limited by simply enlarging the beam spot size.

ACKNOWLEDGMENTS

We thank A. Guarino for having performed preliminary tests of the method, and M. Giglio and L. Formaggia for useful suggestions and discussions. This work has been possible thanks to Italian Ministry of University and Research (MIUR) COFIN 2001 funding.

REFERENCES

1. J. V. Tyrrell, *Diffusion and Heat Flow in Liquids* (Butterworth, London, 1961).
2. S. R. De Groot and P. Mazur, *Nonequilibrium Thermodynamics* (North Holland, Amsterdam, 1962).
3. A. La Porta and C. M. Surko, "Convective instability in a fluid mixture heated from above," Phys. Rev. Lett. **80**, 3759–3762 (1998).
4. R. W. Schmitt, "The ocean's salt fingers," Sci. Am. **272**, 70–75 (1995).
5. L. L. Zheng, D. J. Larson, Jr., and H. Zhang, "Role of thermotransport (Soret effect) in macrosegregation during eutectic/off-eutectic directional solidification," J. Cryst. Growth **191**, 243–251 (1998).
6. R. T. Cygan and C. R. Carrigan, "Time-dependent Soret transport: applications to brine and magma," Chem. Geol. **95**, 201–212 (1992).
7. F. H. Busse, "Fundamentals of thermal convection," in *Mantle Convection: Plate Tectonics and Global Dynamics*, W. Peltier, ed. (Gordon and Breach, London, 1989), pp. 23–95.
8. M. C. Cross and P. C. Honenberg, "Pattern formation outside of equilibrium," Rev. Mod. Phys. **65**, 851–1112 (1993).
9. A. Vailati and M. Giglio, "Nonequilibrium fluctuations in time-dependent diffusion processes," Phys. Rev. E **58**, 4361–4371 (1998).
10. D. Braun and A. Libschaber, "Trapping of DNA by thermophoretic depletion and convection," Phys. Rev. Lett. **89**, 188103 (2002).
11. R. Piazza and A. Guarino, "Soret effect in interacting micellar solutions," Phys. Rev. Lett. **88**, 208302 (2002).
12. S. Iacopini and R. Piazza, "Thermophoresis in protein solutions," Europhys. Lett. **63**, 247–253 (2003).
13. M. Giglio and A. Vendramini, "Soret-type motion of macromolecules in solution," Phys. Rev. Lett. **38**, 26–30 (1977).
14. W. Köhler, "Thermodiffusion in polymer solutions as observed by forced Rayleigh scattering," J. Chem. Phys. **98**, 660–668 (1993).
15. J. P. Gordon, R. C. C. Leite, R. S. Moore, S. P. S. Porto, and J. R. Whinnery, "Long-transient effects in lasers with inserted liquid samples," J. Appl. Phys. **36**, 3–8 (1965).
16. J. R. Whinnery, D. T. Miller, and F. Dabby, "Thermal convection and spherical aberration distortion of laser beams in low-loss liquids," IEEE J. Quantum Electron. **3**, 382–383 (1967).
17. S. E. Bialkowski, *Photothermal Spectroscopy Methods for Chemical Analysis* (Wiley, New York, 1996).
18. M. Franko and C. D. Tran, "Analytical thermal lens instrumentation," Rev. Sci. Instrum. **67**, 1–18 (1996).
19. M. Giglio and A. Vendramini, "Thermal lens effect in a binary liquid mixture: a new effect," Appl. Phys. Lett. **25**, 555–557 (1974).
20. L. Mistura, "Critical behavior of transport coefficients in multicomponent fluid mixtures," J. Chem. Phys. **62**, 4571–4572 (1975).

21. S. Alves, A. Bourdon, and A. M. F. Neto, "Generalization of the thermal lens model formalism to account for thermodiffusion in a single-beam Z-scan experiment: determination of the Soret coefficient," J. Opt. Soc. Am. B **20**, 713–718 (2003).
22. N. Arnaud and J. Georges, "On the analytical use of the Soret-enhanced thermal lens signal in aqueous solutions," Anal. Chim. Acta **445**, 239–244 (2001).
23. S. J. Sheldon, L. V. Knight, and J. M. Thorne, "Laser-induced thermal lens effect: a new theoretical model," Appl. Opt. **21**, 1663–1669 (1982).
24. S. Wu and N. J. Dovichi, "Fresnel diffraction theory for steady-state thermal lens measurements in thin films," J. Appl. Phys. **67**, 1170–1182 (1990).
25. S. A. Akhmanov, D. P. Krindach, A. V. Migulin, A. P. Sukhorukov, and H. V. Khokhlov, "Thermal self-actions of laser beams," IEEE J. Quantum Electron. **4**, 568–575 (1968).
26. L. Quartapelle, *Numerical Simulations of the Incompressible Navier–Stokes Equations* (Birkhauser-Verlag, Berlin, 1993).
27. C. A. Carter and J. M. Harris, "Comparison of models describing the thermal lens effect," Appl. Opt. **23**, 476–481 (1984).
28. M. Giglio and A. Vendramini, "Thermal-diffusion measurements near a consolute critical point," Phys. Rev. Lett. **34**, 561–564 (1975).
29. J. Rauch and W. Köhler, "Diffusion and thermal diffusion in semidilute to concentrated solutions of polystyrene in toluene in the vicinity of the glass transition," Phys. Rev. Lett. **88**, 185901 (2002).